TRANSITION MECHANISM BEHIND A BACKWARD-FACING STEP IN A SUPERSONIC FLOW

Weibo Hu
Faculty of Aerospace Engineering
Delft University of Technology
Kluyverweg 1, 2629HS, Delft, The Netherlands
W.Hu-2@tudelft.nl

Stefan Hickel
Faculty of Aerospace Engineering
Delft University of Technology
Kluyverweg 1, 2629HS, Delft, The Netherlands
S.Hickel@tudelft.nl

Bas van Oudheusden
Faculty of Aerospace Engineering
Delft University of Technology
Kluyverweg 1, 2629HS, Delft, The Netherlands
B.W.vanOudheusden@tudelft.nl

ABSTRACT

The path of laminar-to-turbulent transition behind a backward-facing step (BFS) in the supersonic regime at $Ma = 1.7$ and $Re_{\delta_0} = 13718$ is investigated using a very well-resolved large eddy simulation (LES). Five distinct stages are identified in the transition process by the visualisation of instantaneous flow. The transition is initiated by a Kelvin-Helmholtz (K-H) instability of the separated shear layer, followed by secondary modal instabilities of the distorted K-H vortices, leading to Λ-shaped vortices, hair-pin vortices and finally to a fully turbulent state around the reattachment location. Spectral analysis and proper orthogonal decomposition (POD) reveal that the low-frequency breathing dynamics also plays a major role in the transition process.

INTRODUCTION

The flow dynamics over a BFS has attracted extensive attention in the past decades, as it is not only an appealing prototype for studying the separation, recirculation and reattachment behavior in the view of its geometrical simplicity, but also for investigating the transition from laminar to turbulent flow without artificial disturbances (Kostas *et al.*, 2002; Lanzerstorfer & Kuhlmann, 2012). There is a considerable amount of experimental and numerical work about the development of flow instability in the subsonic flow (Marquet *et al.*, 2008; Duncan Jr, 2014). The conclusion drawn is that several distinct mechanisms, like centrifugal, lift-up effects or K-H instability, play a major role in the transition behind the step (Theofilis, 2011).

In the supersonic regime, however, there are additional mechanisms related to compressibility and the occurrence of compression waves at flow reattachment (Tihon *et al.*, 2001; Sriram & Chakraborty, 2011). Thereby, it is reasonable to conjecture that a different mechanism may contribute to the transition process in the supersonic case. The main objective of the current investigation is to characterize the transition process behind a BFS by scrutinizing the evolution of instantaneous vortical structures.

NUMERICAL SETUP

The setup for the current study is an open BFS (no upper wall) with supersonic laminar inlet boundary conditions at $Ma = 1.7$ and $Re_{\delta_0} = 13718$ based on the inlet boundary layer thickness δ_0 and free-stream viscosity. The size of the computational domain is $(L_x,\ L_y,\ L_z) = \big([-40,70],[-3,30],[-2.5,2.5]\big)\delta_0$ with a step height of $h = 3\delta_0$. The main flow parameters are summarized in Table 1. At the domain inlet, a clean laminar boundary layer profile is imposed. The step and wall are modeled as non-slip adiabatic surfaces. All flow variables are extrapolated at the outlet of the domain. On the top of the domain, non-reflecting boundary conditions based on Riemann invariants are used. Periodic boundary conditions are enforced in the spanwise direction. We employ the implicit large eddy simulation (ILES) method of Hickel *et al.* (2014) for solving the compressible Navier-Stokes equations, which has been successfully applied to various supersonic cases, such as shock wave/boundary layer interactions (SWBLI) on a compression ramp (Grilli *et al.*, 2012) and a flat plate (Pasquariello *et al.*, 2017). More details about the numerical method can be found in Hickel *et al.* (2006, 2014).

RESULTS AND DISCUSSION

Mean flow organization

The main flow features are visualized by the time- and spanwise-averaged flow field in Figure 1. The incoming flow experiences a centered Prandtl-Meyer expansion and separates at the step corner. Then the free shear layer develops towards the downstream wall and finally impinges on the wall surface. Compression waves are generated at the reattachment location and then coalesce into a reattachment shock (white solid line). The low-speed recirculating flow forms a separation bubble underneath the dividing line (here defined for convenience as the isoline of $u = 0$ indicated by the black dashed line), while the high-speed flow proceeds downstream by overcoming the reattachment pressure rise. The mean reattachment length is about $L_r = 10.9\delta_0$ ($3.6h$), which is consistent with the previous results at similar con-

Table 1. Main flow parameters of the current case

Ma_∞	U_∞	δ_0	Re_∞	T_0	p_0	h	p_∞
1.7	469.85 m/s	1 mm	$1.3718 \times 10^7\ \mathrm{m}^{-1}$	300 K	1×10^5 Pa	3 mm	20 259 Pa

ditions, reporting that the reattachment length is usually within $3.0 \sim 4.0h$ around the current Mach number (Karimi *et al.*, 2012). Downstream of the reattachment point, the distance between the sonic line (white dashed line) and wall decreases with the streamwise distance as a result of the increasing velocity gradient near the wall, which indicates the development towards a fully turbulent boundary layer.

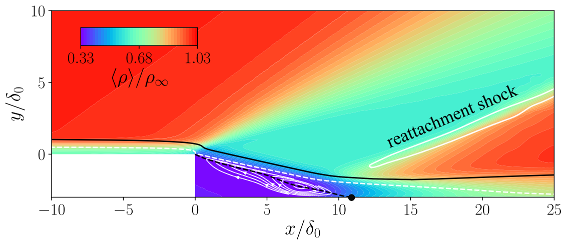

Figure 1. Time- and spanwise-averaged contour of density. The solid circle (•) indicates the mean reattachment point. The white dashed and solid lines denote the isolines of $Ma = 1.0$ and $|\nabla p|\delta_0/p_\infty = 0.24$. The black dashed and solid lines signify isolines of $u = 0.0$ and $u/u_e = 0.99$.

The separation length is further confirmed by the mean skin friction distribution in Figure 2(a), where $\langle C_f \rangle$ represents the skin friction normalized by $0.5\rho_\infty U_\infty^2$. The intensity of separated flow is not uniform as $\langle C_f \rangle$ varies with streamwise distance along the separation bubble. The level of $\langle C_f \rangle$ remains almost zero in the upstream part of the separation bubble ($0 < x/\delta_0 < 6.3$), which is followed by a decrease of $\langle C_f \rangle$ towards a global minimum at $x/\delta_0 = 8.4$. Then $\langle C_f \rangle$ slowly climbs up and eventually stays steady at about $\langle C_f \rangle = 2.9 \cdot 10^{-3}$ for $x/\delta_0 > 25$, which is a typical level of a turbulent boundary layer at this Reynolds number range. The trend and level of $\langle C_f \rangle$ match well with the numerical results of Spazzini *et al.* (2001) despite the different inlet boundary conditions and reattachment length.

The wall pressure in Figure 2(b) displays a sharp drop by about 50% in front of the step. The wall pressure then gradually reduces further to reach its global minimum at $x/\delta_0 = 7.3$ in the separation bubble. In terms of the trend and relative variation, our results are in good agreement with the numerical works of Karimi *et al.* (2012). The three inflection points of the wall-pressure distribution are considered to be associated with the separation, emergence of compression waves and reattachment, respectively, as reported in Délery *et al.* (1986).

The boundary layer state can be characterized basically by the evolution of the wall-normal velocity profile along the streamwise direction shown in Figure 3, where $\Delta y/\delta_0$ signifies the normalized wall distance. Sufficiently upstream of the step edge, the velocity profile corresponds to a typical laminar boundary layer. At the step corner ($x/\delta_0 = 0$), the streamwise velocity gradient increases significantly due to the separation caused by the sharp expansion of the geometry. It is noticeable that there exist two inflection points in the velocity profile at this location, which implies the boundary layer features strong inviscid instability at the step. The main streamwise velocity increases across the expansion due to the favorable pressure gradient, see also Figure 2(b). Compared to the upstream velocity profile, the boundary layer profile displays a large momentum deficit in the separated region, for example, at $x/\delta_0 = 5$ there is a small reverse velocity observed with corresponding velocity deficit of about $1.0u_\infty$ extending over $0 \leq \Delta y/\delta_0 \leq 1.5$. Also shortly downstream of reattachment (which takes places near $x/\delta_0 = 11$), we find two inflection points in the velocity profile at $x/\delta_0 = 15$, which shows that the boundary layer has not yet reached an equilibrium state. The outer flow velocity gradually returns to its initial level with the recompression across behind the reattachment shock, see Figure 2(b). The flattening of the velocity profile and steeper velocity gradient near the wall, compared to the upstream velocity profile, both indicate the development of the turbulent boundary layer.

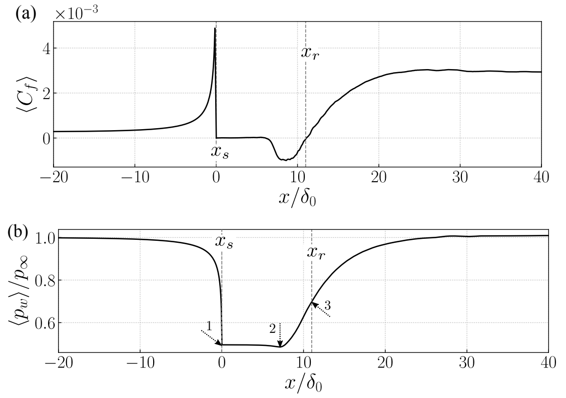

Figure 2. Time- and spanwise-averaged (a) skin friction and (b) wall pressure. The dashed lines indicate the averaged separation and reattachment location.

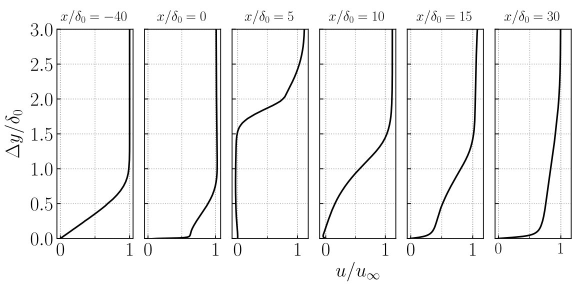

Figure 3. Streamwise evolution of spanwise- and time-averaged streamwise velocity profile. Note: The y-axis is the non-dimensional normal distance from the wall.

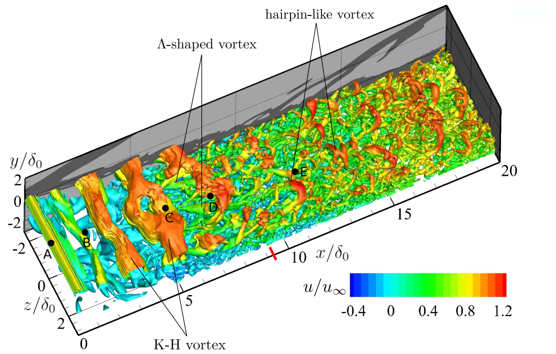

Figure 4. Instantaneous vortical structures at $tu_\infty/\delta_0 = 793$, visualized by isosurfaces of $\lambda_2 = -0.005$. The black shade represents the contour of $|\nabla p|\delta_0/p_\infty = 0.24$ at the slice $z/\delta_0 = -2.5$. The red solid line signifies the instantaneous spanwise-averaged reattachment point. The five stages are marked as A, B, C, D, E, respectively.

Transition Process

The instantaneous vortical structures in a typical flow realization are visualized by means of the λ_2 vortex criterion in Figure 4. We can identify five distinct stages of the transition process based on the appearance of the vortical structures. The first stage is the relatively short range where two-dimensional spanwise structures are initiated due to the inviscid K-H instability of the shear layer.

In the second stage, the spanwise structures evolve further into large quasi two-dimensional vortices. These clockwise rotating spanwise-aligned K-H vortices are subsequently deforming into oblique waves as a result of their secondary instability triggered by small horseshoe vortices beneath as the free shear layer flow develops downstream.

The streamwise velocity is not distributed uniformly along the oblique waves, which induces the formation of low and high momentum zones along the spanwise direction. With the spanwise modulation of the wavy vortices, the low-momentum parts form into the legs of a Λ-shaped vortex structure and the high-momentum parts develop into the head of a Λ-shaped vortex in the third stage. At the same time, the distorted vortices pair with each other since the high-speed part of upstream vortices catches up with the low-speed part of downstream vortices. The separated shear layer flow thus exhibits the formation of large-scale vortices via K-H and secondary instability, and then these vortices keep stretching, pairing and begin to break down as the shear layer evolves, similar as reported by Schäfer *et al.* (2009) for their incompressible case.

In the next stage, the large coherent Λ-shaped vortices break down into several small Λ-shaped vortices staggered in the spanwise direction due to the streamwise stretching of vortices, in which the head part of the vortex (relatively far away from the wall) is convected faster than the leg parts until this behavior tears down the large vortex. Emerging smaller Λ-shaped vortices indicate the onset of the nonlinear regime, which originates from the upstream self-excited quasi-periodical K-H vortices, instead of the natural spanwise differential amplification of the Tollmien-Schlichting (T-S) waves (Herbert, 1988). There also exist low-momentum zones in the leg parts and high-momentum zones in the head parts of the small Λ-shaped vortices.

In the last stage, the vortex-stretching mechanism continues so that the legs of Λ-shaped vortex are elongated. The hairpin vortices appear to be lifted up caused by the stretched legs in the wall-normal direction (Cherubini *et al.*, 2011). This rolling up event contributes to the formation of large hairpin vortices, which is the signature of turbulent boundary layer flow.

In this transition process, we do not observe Görtler vortex pairs. The Görtler instability can be quantified by the non-dimensional Görtler number G_t, whose local value is computed along the boundary layer edge. We found that it remains below the threshold $G_t = 0.58$ (Smits & Dussauge, 2006) at every x coordinate upstream of the mean reattachment location where significant turbulence is already observed. Therefore, we conclude that the Görtler instability does not play a role in this transitional case.

For each stage of the transition process, spanwise profiles of the fluctuations of the streamwise velocity are shown in Figure 5 (note the smaller scale for the first two stations). We can clearly see the differences in the dimensional features of the traveling waves in each stage. In the first stage, the spanwise waves are completely two-dimensional and their wavelength is about half of the spanwise domain size, Figure 5(a). Then these two-dimensional waves modulate into oblique waves and their amplitudes increase by approximately one order, Figure 5(b). The three-dimensional features of the unstable waves are obvious and their fluctuations become more energetic in the following three stages. As reviewed by Herbert (1985), the vortex pairing process is usually observed in inflectional boundary layers at very large amplitudes of the periodic modulation. It seems that the three-dimensional characteristics of the unstable waves emerge in a short distance behind the step and soon become highly energetic before reaching half of the separation length.

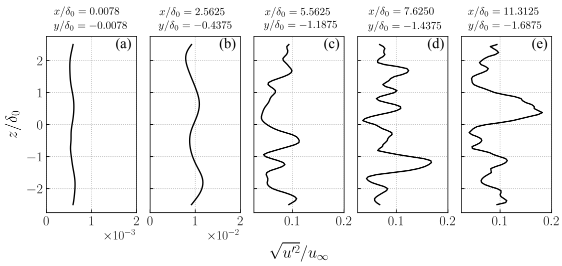

Figure 5. Fluctuations of streamwise velocity along the spanwise direction at five different locations shown in Figure 4 (marked as A, B, C, D and E). Each of them corresponds to one stage of the transition process.

The root-mean-square (RMS) and amplification factor of the streamwise velocity fluctuations are plotted as function of the streamwise distance through the fives stages of the transition in Figure 6. Based on the profile of streamwise velocity RMS at a specific x_i location, we find y_i where the local profile has the maximum. The position (x_i, y_i) is considered to be the local most unstable point and computed along the streamwise direction. The RMS of the streamwise velocity we display (solid line) are the results at these locations (x_i, y_i). Then we compute the perturbation amplitudes A_i from the time series data at (x_i, y_i). The amplification factor is normalized based on the amplitude A_0 at $x = 0$. The level of fluctuations grows smoothly in the first two stages and experiences an accelerated growth caused by the secondary instability and vortex breakdown in the third and fourth stages (solid line in Figure 6). The streamwise modulation of low and high momentum parts of Λ-shaped vortices also contributes to the accelerated growth. In the last stage, the fluctuations reach their maximum around the reattachment point ($x/\delta_0 = 10.9$) and gradually return to an almost constant level in the turbulent boundary layer (not shown in the figure). Concerning the amplification factor (dashed line), at first, the amplitude of fluctuations displays a rapid modal growth of K-H vortices, in agreement with the stability analysis by Reshotko & Tumin (2001). In the next two stages, the growth rate (represented by the slope of the amplification factor) is much smaller than before although the amplification factor still slowly increases. The amplification factor continues increasing because of a rapid onset of non-linear distortion and breakdown to turbulence in the fourth stage. In the last stage, the amplification factor almost keeps steady at a high level.

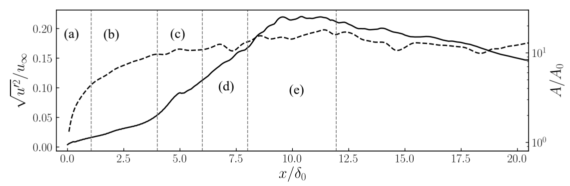

Figure 6. RMS (solid line) and amplification factor (dashed line) of streamwise velocity fluctuations along streamwise direction through the five stages of the transition in Figure 4 based on the spanwise-averaged flow field.

In conclusion, the above visualization and analysis show rapid modal growth of K-H type transition right behind the step. The amplitude of fluctuations exceeds $0.1\% u_\infty$ after a short distance from the step, which indicates that nonlinear interactions become important rather than T-S instability. Therefore, we believe the transition process consists of onset and modal growth of K-H vortices (stage 1, 2), secondary instability (stage 3), breakdown of the large coherent vortices (stage 4) and turbulent state (stage 5).

Spectral Analysis

In order to highlight the relative contributions of different mechanisms to the transition, the dynamic behavior is characterized by means of the frequency weighted power spectral density (FWPSD) of the pressure (normalized by the local integral values $\int P(f)\mathrm{d}f$) along the dividing line, as shown in Figure 7. The time signals are extracted in time ranges $tu_\infty/\delta_0 = 800 \sim 1150$ with a sampling frequency $f_s\delta_0/u_\infty = 2$, as the frequencies above the characteristic frequency of the turbulent integral scales u_∞/δ_0 are not of our current interest. In the first stage, the separated shear layer features a significant low-frequency oscillation with $f\delta_0/u_\infty \approx 0.02$ immediately behind the step. This unsteady behavior is believed to be associated with the breathing motion of the separation bubble, as we have discussed in our previous work (Hu *et al.*, 2019). The dominant frequency then shifts towards higher values of $f\delta_0/u_\infty \approx 0.2$ in the second stage, where the oblique K-H vortices are observed. Although we can infer that there is still low-frequency breathing unsteadiness in this stage, the dominant frequency is around the characteristic frequency

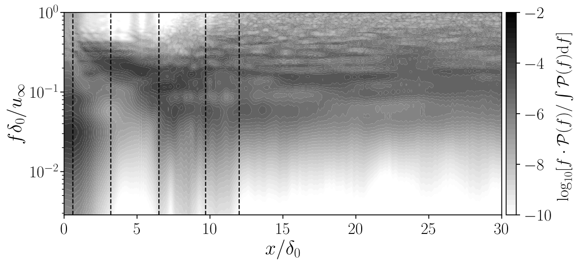

Figure 7. Frequency weighted power spectral density map of pressure signals along the dividing line based on $z = 0$ slice. The weighted spectra are normalized by $\int P(f)\mathrm{d}f$ at every streamwise location. The five stages of the transition process are indicated by vertical dashed lines.

of the K-H vortices which underlines the important role of the K-H instability in the transition scenario. As the shear layer develops, the most energetic content of the shear layer gradually shifts to lower frequencies in the following stages ($3.2 < x/\delta_0 < 12$), and evolves towards a broadband frequency spectrum. Downstream the transition region ($x/\delta_0 \geq 12$), the fluctuations in the turbulent boundary layer are distributed over the full spectrum without a clear preferred frequency.

Proper Orthogonal Decomposition

A modal decomposition of the flow field is carried out based on proper orthogonal decomposition (POD). POD extracts the most energetic modes in an orthogonal space, which can be used to reconstruct the main flow features of the interactions between the vortices, reattachment and shock waves.

The current POD for both velocity and pressures is conducted based on $N = 700$ equal-interval snapshots of the spanwise-averaged flow field from $tu_\infty/\delta_0 = 800$ to 1150 with a sample frequency of $f_s\delta_0/u_\infty = 2$, which corresponds to a frequency resolution of $2.9 \cdot 10^{-3} < St_{\delta_0} < 1$. In Figure 8, we give the POD energy spectrum of the first 90 modes resulting from the snapshots method. The fraction of the energy for each mode E_i and the corresponding accumulative energy sum ES_i are defined as follows:

$$E_i = (\lambda_i / \sum_{k=1}^{N} \lambda_k) \times 100 \tag{1}$$

$$ES_i = (\sum_{j=1}^{i} \lambda_j)/(\sum_{k=1}^{N} \lambda_k) \tag{2}$$

These 90 modes are selected based on the accumulative energy sum ES_i being larger than 80%. If an individual mode occupies more energy of the whole energy spectrum, it usually is assumed to more important for flow dynamics.

Based on the energy fraction spectrum (Figure 8), we scrutinize the features of first eighteen modes to identify the leading unstable flow structures. The contribution of each individual mode to the coherent structure does not only depend on the amount of the relative disturbance energy, but also on the interactions between the POD modes and the evolution of the specific flow instability. These eighteen

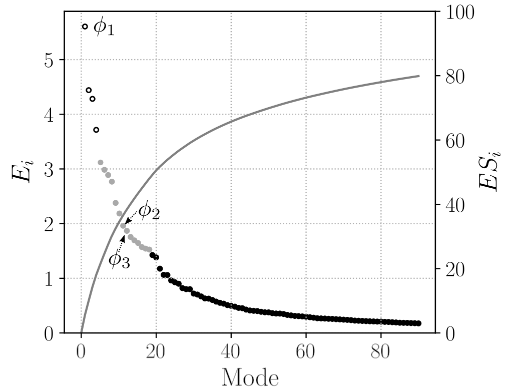

Figure 8. Energy spectrum of the first 90 POD modes of the pressure fluctuations. The black hollow circles signify the first branch and the gray solid circles indicate the second branch.

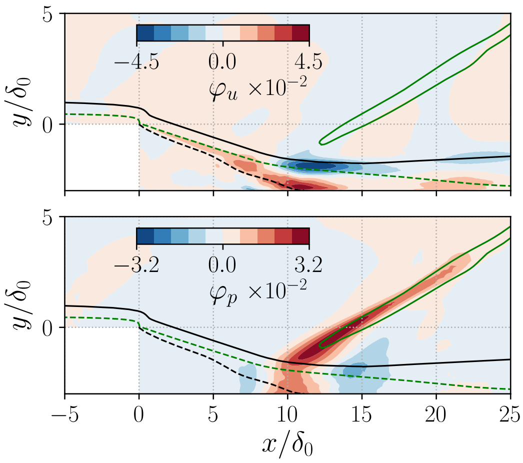

Figure 9. POD mode ϕ_1 showing contours of (a) the streamwise velocity and (b) pressure fluctuations. The green solid and dashed line indicate the mean reattachment shock and sonic line. The black solid and dashed line signify the boundary layer edge and dividing line.

modes can be categorized as two branches based on their features shown by the velocity and pressure fluctuations in the following section.

In the first branch (represented by the black hollow circles in Figure 8), we select one mode, marked as ϕ_1, to illustrate the corresponding main flow dynamics. In Figure 9, we show the streamwise velocity and pressure fluctuations from the most energetic mode ϕ_1. The velocity disturbances of ϕ_1 are mainly located in the reattachment point of the separation flow, while the pressure fluctuations are distributed along the reattachment shock. We consider therefore that mode ϕ_1 is associated with the interaction between the separation bubble and reattachment shock, which contributes relatively more to the transition in the whole process.

The selected modes in the second branch (denoted by the gray solid circles in Figure 8) are labeled as mode ϕ_2 and ϕ_3. These two modes appear to have $\pi/2$ phase difference, which describes the convection or shedding behavior (van Oudheusden *et al.*, 2005), as shown in Figures 10

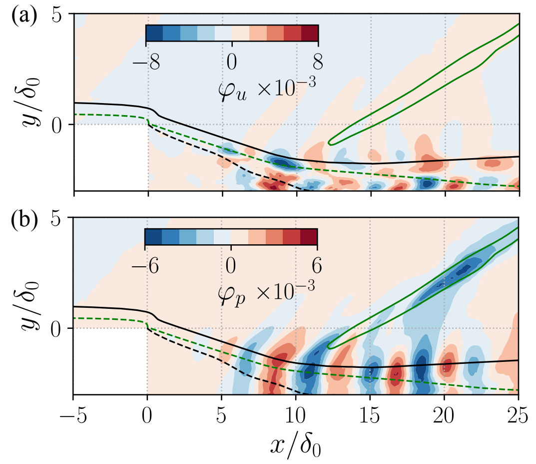

Figure 10. POD mode ϕ_2 showing contours of (a) the streamwise velocity and (b) pressure fluctuations. Significations of lines are the same as in Figure 9.

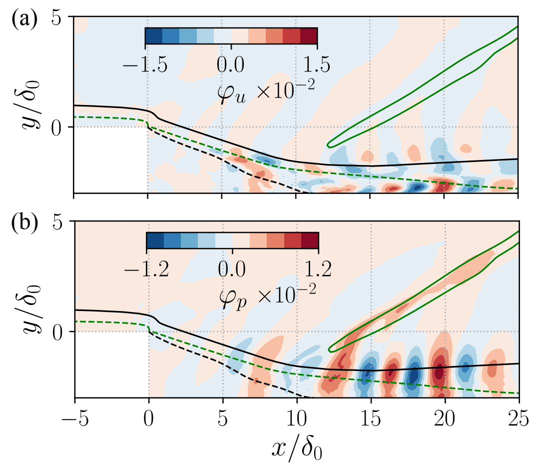

Figure 11. POD mode ϕ_3 showing contours of (a) the streamwise velocity and (b) pressure fluctuations. Significations of lines are the same as in Figure 9.

and 11. These two modes are related to the shedding of K-H vortices because both velocity and pressure fluctuations are characterized with alternative negative and positive values along the shear layer region. Although these two modes contains less energy than mode ϕ_1, they still have an important impact on the transition, especially in the stage 2 and 3, as we observed in Figure 7. Thereby we consider that both interaction system and the K-H vortices have effects on the development of the flow instability.

Conceptual Model

The above instantaneous flow visualizations provide a clear view of the transition process, which is summarized in the schematic in Figure 12. Five distinct stages are identified in the transition process. At the first stage, upon separation a quasi-steady two-dimensional shear layer is formed subject to K-H instability. The breathing behavior of the bubble is the main driving force of the large-scale unsteadiness of the separated flow region. Then clockwise rotating spanwise vortices are induced by the K-H instability. These K-H vortices grow rapidly and are subsequently deforming

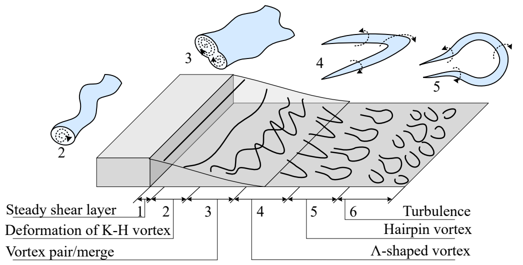

Figure 12. Conceptual model of the transition process in the supersonic BFS.

as a result of the secondary instability in the second stage. The traveling velocity of the wavy K-H vortices varies in the spanwise direction and thus spanwise modulation occurs (third stage). The high-speed parts develop into the head of Λ-shaped vortex and the low-speed parts develop into the legs parts. In these two stages, the K-H instability appears to dominate the transition. At the fourth stage, the large coherent vortices break down into several small Λ-shaped vortices caused by the streamwise stretching of vortices and the reattachment event. Then they roll up and develop into larger hairpin vortices in the last phase, which is the signature of the turbulent boundary layer. Given the rapid modal growth of the disturbances behind the step and high levels of the amplitudes, we believe the nonlinear behavior is significant in the transition process, which involves the breathing behavior of the separation bubble, the modal growth of the K-H and secondary instability, vortex breakdown and eventually fully developed turbulence in the current case.

CONCLUSION

The current work numerically investigates the transition path of a BFS in a laminar flow at $Ma = 1.7$ and Re_{δ_0}. The transition process involves modal growth of K-H and secondary instability, and relative nonlinear dynamics, which plays important roles through the transition path. The K-H instability is the main driver of the transition in the second and third stage of the transition. In the meantime, the low-frequency breathing interaction system also contributes to the transition.

REFERENCES

Cherubini, S., De Palma, P., Robinet, J. C. & Bottaro, A. 2011 The minimal seed of turbulent transition in the boundary layer. *J. Fluid Mech.* **689**, 221–253.

Délery, J., Marvin, J. G .& Reshotko, E. 1986 Shock-wave boundary layer interactions. *Tech. Rep.*. Advisory Group for Aerospace Research and Development, AGARD-AG-280.

Duncan Jr, G. T. 2014 The effects of step excrescences on swept-wing boundary-layer transition. PhD thesis, Texas A & M University.

Grilli, M., Schmid, P. J., Hickel, S. & Adams, N. A. 2012 Analysis of unsteady behaviour in shockwave turbulent boundary layer interaction. *J. Fluid Mech.* **700**, 16–28.

Herbert, T. 1985 Three-dimensional phenomena in the transitional flat-plate boundary layer. In *AIAA 23rd Aerosp. Sci. Meet.*. Reno, Nevada: AIAA 85-0489.

Herbert, T. 1988 Secondary instability of boundary layers. *Annu. Rev. Fluid Mech.* **20** (1), 487–526.

Hickel, S., Adams, N. A. & Domaradzki, J. A. 2006 An adaptive local deconvolution method for implicit LES. *J. Comput. Phys.* **213** (1), 413–436.

Hickel, S., Egerer, C. P. & Larsson, J. 2014 Subgrid-scale modeling for implicit large eddy simulation of compressible flows and shock-turbulence interaction. *Phys. Fluids* **26** (10), 106101.

Hu, W., Hickel, S. & van Oudheusden, B. W. 2019 Shock wave-boundary layer interaction in a transitional flow over a backward-facing step. In *54th 3AF Int. Conf. Appl. Aerodyn.*. Paris, France.

Karimi, A., Wijeyakulasuriya, S. & Nalim, M. 2012 Numerical study of supersonic flow over backward-facing step for scramjet application. In *48th AIAA/ASME/SAE/ASEE Jt. Propuls. Conf. Exhib.*. Atlanta, Georgia: AIAA 2012-4001.

Kostas, J., Soria, J. & Chong, M. 2002 Particle image velocimetry measurements of a backward-facing step flow. *Exp. Fluids* **33** (6), 838–853.

Lanzerstorfer, D. & Kuhlmann, H. C. 2012 Three-dimensional instability of the flow over a forward-facing step. *J. Fluid Mech.* **695**, 390–404.

Marquet, O., Sipp, D., Chomaz, J. M. & Jacquin, L. 2008 Amplifier and resonator dynamics of a low-Reynolds-number recirculation bubble in a global framework. *J. Fluid Mech.* **605**, 429–443.

van Oudheusden, B. W., Scarano, F., van Hinsberg, N. P. & Watt, D. W. 2005 Phase-resolved characterization of vortex shedding in the near wake of a square-section cylinder at incidence. *Exp. Fluids* **39** (1), 86–98.

Pasquariello, V., Hickel, S. & Adams, N. A. 2017 Unsteady effects of strong shock-wave/boundary-layer interaction at high Reynolds number. *J. Fluid Mech.* **823**, 617–657.

Reshotko, E. & Tumin, A. 2001 Spatial theory of optimal disturbances in a circular pipe flow. *Phys. Fluids* **13** (4), 991–996.

Schäfer, F., Breuer, M. & Durst, F. 2009 The dynamics of the transitional flow over a backward-facing step. *J. Fluid Mech.* **623**, 85.

Smits, A. J. & Dussauge, J. P. 2006 *Turbulent shear layers in supersonic flow*. Springer Science & Business Media.

Spazzini, P. G., Iuso, G., Onorato, M., Zurlo, N. & Di Cicca, G. M. 2001 Unsteady behavior of back-facing step flow. *Exp. Fluids* **30** (5), 551–561.

Sriram, A. & Chakraborty, D. 2011 Numerical exploration of staged transverse injection into confined supersonic. *Def. Sci. J.* **61** (1), 3–11.

Theofilis, V. 2011 Global Linear Instability. *Annu. Rev. Fluid Mech.* **43** (1), 319–352.

Tihon, J., Legrand, J. & Legentilhomme, P. 2001 Near-wall investigation of backward-facing step flows. *Exp. Fluids* **31** (5), 484–493.